



HAL
open science

A-type stars in the Canada–France Imaging Survey I. The stellar halo of the Milky Way traced to large radius by blue horizontal branch stars

Guillaume F. Thomas, Alan Mcconnachie, Rodrigo Ibata, Patrick Côté,
Nicolas Martin, Else Starkenburg, Raymond Carlberg, Scott Chapman,
Sébastien Fabbro, Benoit Famaey, et al.

► **To cite this version:**

Guillaume F. Thomas, Alan Mcconnachie, Rodrigo Ibata, Patrick Côté, Nicolas Martin, et al.. A-type stars in the Canada–France Imaging Survey I. The stellar halo of the Milky Way traced to large radius by blue horizontal branch stars. *Monthly Notices of the Royal Astronomical Society*, 2018, 481 (4), pp.5223-5235. 10.1093/mnras/sty2604 . hal-02306458

HAL Id: hal-02306458

<https://hal.science/hal-02306458>

Submitted on 23 Feb 2023

HAL is a multi-disciplinary open access archive for the deposit and dissemination of scientific research documents, whether they are published or not. The documents may come from teaching and research institutions in France or abroad, or from public or private research centers.

L'archive ouverte pluridisciplinaire **HAL**, est destinée au dépôt et à la diffusion de documents scientifiques de niveau recherche, publiés ou non, émanant des établissements d'enseignement et de recherche français ou étrangers, des laboratoires publics ou privés.

A-type stars in the Canada–France Imaging Survey I. The stellar halo of the Milky Way traced to large radius by blue horizontal branch stars

Guillaume F. Thomas,^{1★} Alan W. McConnachie,¹ Rodrigo A. Ibata,² Patrick Côté,¹ Nicolas Martin,^{2,3} Else Starkenburg,⁴ Raymond Carlberg,⁵ Scott Chapman,⁶ Sébastien Fabbro,¹ Benoit Famaey,² Nicholas Fantin,¹ Stephen Gwyn,¹ Vincent Hénault-Brunet,¹ Khyati Malhan,² Julio Navarro,⁷ Annie C. Robin⁸ and Douglas Scott⁹

¹*NRC Herzberg Astronomy and Astrophysics, 5071 West Saanich Road, Victoria, BC V9E 2E7, Canada*

²*Université de Strasbourg, CNRS, Observatoire astronomique de Strasbourg, UMR 7550, F-67000 Strasbourg, France*

³*Max-Planck-Institut für Astronomie, Königstuhl 17, D-69117 Heidelberg, Germany*

⁴*Leibniz Institute for Astrophysics Potsdam (AIP), An der Sternwarte 16, D-14482 Potsdam, Germany*

⁵*Department of Astronomy and Astrophysics, University of Toronto, Toronto, ON M5S 3H4, Canada*

⁶*Department of Physics and Atmospheric Science, Dalhousie University, Coburg Road, Halifax, NS B3H 1A6, Canada*

⁷*Department of Physics and Astronomy, University of Victoria, Victoria, BC V8P 1A1, Canada*

⁸*Institut UTINAM, CNRS UMR6213, Univ. Bourgogne Franche-Comté, OSU THETA Franche-Comté-Bourgogne, Observatoire de Besançon, BP 1615, F-25010 Besançon Cedex, France*

⁹*Department of Physics and Astronomy, University of British Columbia, Vancouver, BC V6T 1Z1, Canada*

Accepted 2018 September 19. Received 2018 September 18; in original form 2018 May 31

ABSTRACT

We present the stellar density profile of the outer halo of the Galaxy traced over a range of Galactocentric radii in the range $15 < R_{GC} < 220$ kpc by blue horizontal branch (BHB) stars. These stars are identified photometrically using deep *u*-band imaging from the new Canada–France Imaging Survey (CFIS) that reaches 24.5 mag. This is combined with *griz* bands from Pan-STARRS 1 and covers a total of ~ 4000 deg² of the northern sky. We present a new method to select BHB stars that has low contamination from blue stragglers and high completeness. We use this sample to measure and parametrize the three-dimensional density profile of the outer stellar halo. We fit the profile using (i) a simple power law with a constant flattening (ii) a flattening that varies as a function of Galactocentric radius (iii) a broken power-law profile. We find that outer stellar halo traced by the BHB is well modelled by a broken power law with a constant flattening of $q = 0.86 \pm 0.02$, with an inner slope of $\gamma = 4.24 \pm 0.08$. This is much steeper than the preferred outer profile that has a slope of $\beta = 3.21 \pm 0.07$ after a break radius of $r_b = 41.4^{+2.5}_{-2.4}$ kpc. The outer profile of the stellar halo trace by BHB stars is shallower than that recently measured using RR Lyrae, a surprising result given the broad similarity of the ages of these stellar populations.

Key words: stars: distances – stars: horizontal branch – stars: statistics – Galaxy: halo – Galaxy: structure.

1 INTRODUCTION

It is now generally accepted that large galaxies, like the Milky Way, have been formed by a succession of mergers and via the accretion of smaller galaxies, in a process called hierarchical formation. In the case of accretions, the smaller galaxy is disrupted due to the tidal effects generated by the larger (host) galaxy. This leads to the

formation of stellar streams clearly visible around many massive galaxies of the Local Group (e.g. Martínez-Delgado et al. 2010; Martin et al. 2013; Bernard et al. 2016; Grillmair & Carlin 2016; Malhan, Ibata & Martin 2018). Although these structures stay spatially coherent for many Gyr (Johnston et al. 2008), they tend to be eventually destroyed by mixing effects and are in turn assimilated to form part of the ‘smooth’ stellar halo.

The stellar halo of a L^* galaxy can be a complex structure, very inhomogeneous and clumpy. Nevertheless, it is possible to view it as a smooth component with halo substructures, from which we can

★ E-mail: guillaume.thomas@nrc-cnrc.gc.ca

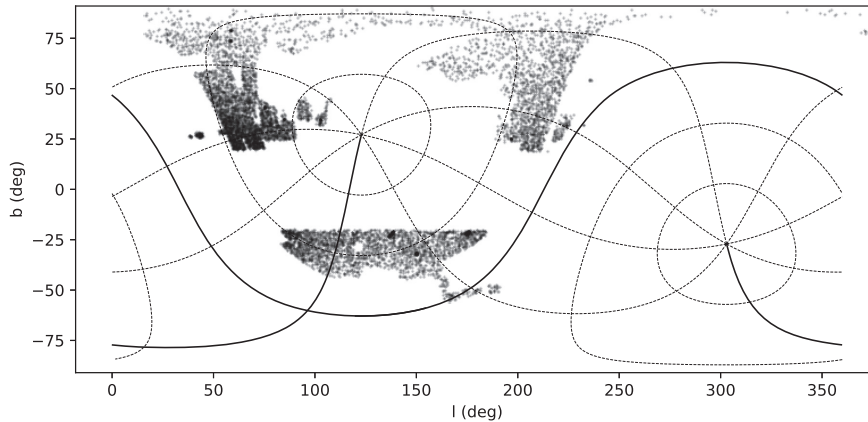


Figure 1. The spatial coverage of CFIS at the time of our study. Specifically, the grey points show the apparent position of the BHBs from our sample. The black lines show the equatorial coordinates, with the equatorial plane highlighted with a solid line.

study the accretion history, in particular of the Milky Way. Indeed, as shown in many cosmological simulations (Bullock & Johnston 2005; Abadi, Navarro & Steinmetz 2006; Johnston et al. 2008; Cooper et al. 2010; Pillepich et al. 2014, 2018; Amorisco 2017), the accretion history of a galaxy has a huge impact on the profile of the smooth stellar halo component, such that galaxies having the most quiescent accretion history tend to have a profile less steep than for a galaxy of the same mass that has had a much more active accretion history (Libeskind et al. 2011). Most studies of the profile of the Milky Way stellar halo do not go beyond ~ 100 kpc, due to the depth of large surveys like the Sloan Digital Sky Survey (SDSS) and the faint absolute magnitude of tracers (Yanny et al. 2000; Bell et al. 2008; Watkins et al. 2009; De Propriis, Harrison & Mares 2010; Pila-Díez et al. 2015; Xue et al. 2015; Slater et al. 2016). Large area surveys are essential in order to gain constraints on the three-dimensional shape of the stellar halo (Cohen et al. 2017; Fukushima et al. 2018).

Blue Horizontal Branch stars (BHB) are ideal tracers for studying the profile of the outer stellar halo ($R_{GC} > 20$ kpc). They are present in old stellar populations, and their absolute magnitude is roughly constant and bright $M_g \simeq 0.5$ (Deason, Belokurov & Evans 2011), meaning that they can be identified even at very large distances (> 100 kpc). SDSS, although covering a large portion of the sky ($\sim 14\,000$ deg 2), does not have a deep enough u band to study the halo beyond 100 kpc (Deason et al. 2014). The new u -band coverage provided by the Canada–France Imaging Survey (CFIS), intended to eventually cover $\sim 10\,000$ deg 2 of the northern hemisphere, is ~ 2.5 mag deeper than the u band of the SDSS (Ibata et al. 2017). It is therefore now possible to study the stellar halo for a large fraction of the sky up to a galactocentric distance of ~ 220 kpc with BHB stars identified in CFIS.

In this article, we study the three-dimensional profile of the outer stellar halo with a sample of BHB stars, selected through their photometry using the CFIS and Pan-STARRS 1 data that we will present in Section 2. Section 3 presents a new method to disentangle BHB stars from other stellar populations, especially the Blue Stragglers (BS), and we determine the distances to our BHB sample (Section 3.2). Then, in Section 4, we present our study of the completeness of the BHB sample, including spatial variations. Section 5 describes our derivation of the radial profile and its parametrization.

Then, in Section 6, we discuss the results and compare our best-fitting parameters with those found in previous work. Finally, we summarize our results in Section 7.

2 DATA

The primary source of observational data used in this study is a merged catalogue using the *griz* bands from Pan-STARRS 1 (Chambers et al. 2016) (hereafter PS1; specifically, we use the forced PSF photometry parameters) and the u band from CFIS (Ibata et al. 2017). The PS1 survey covers more than 3/5 of the sky; as such, the spatial coverage of our merged catalogue is limited by the spatial coverage of the CFIS data at the time of our study (~ 4000 deg 2). CFIS excludes most of the Galactic disc by applying a cut in Galactic latitude at $b < 19$ deg, and the current footprint is limited to a declination of $\delta \leq 60$ deg. The current footprint of the CFIS survey is visible in Fig. 1.

By crossmatching the CFIS and PS1 catalogues, we retain 98 percent of the PS1 detections in the relevant magnitude range.

Following Farrow et al. (2014), we use the following criterion to separate stars from the background galaxies, defined in the PS1 i band:

$$i_{\text{PSF}} - i_{\text{Kron}} < 0.05. \quad (1)$$

It is worth noting that star-galaxy classification done in this way becomes unreliable at $i_{\text{PSF}} \gtrsim 21$; nevertheless, more than 93 percent of the final sample of BHB stars extracted in this survey have $i < 21$, thus star-galaxy misclassification is not expected to have a large impact on the results of this study.

To correct for the Galactic foreground extinction, we used the extinction values, $E(B - V)$, of Schlegel, Finkbeiner & Davis (1998), assuming the conversion factor given by Schlafly & Finkbeiner (2011) for a reddening parameter $R_v = 3.1$. For the u band of the CFIS survey, we have assumed that this coefficient is approximately the same as the coefficient of the u band for SDSS. We limit our data set to have photometric uncertainties < 0.2 mag in each bands ($u, g, r, i, \text{ and } z$).

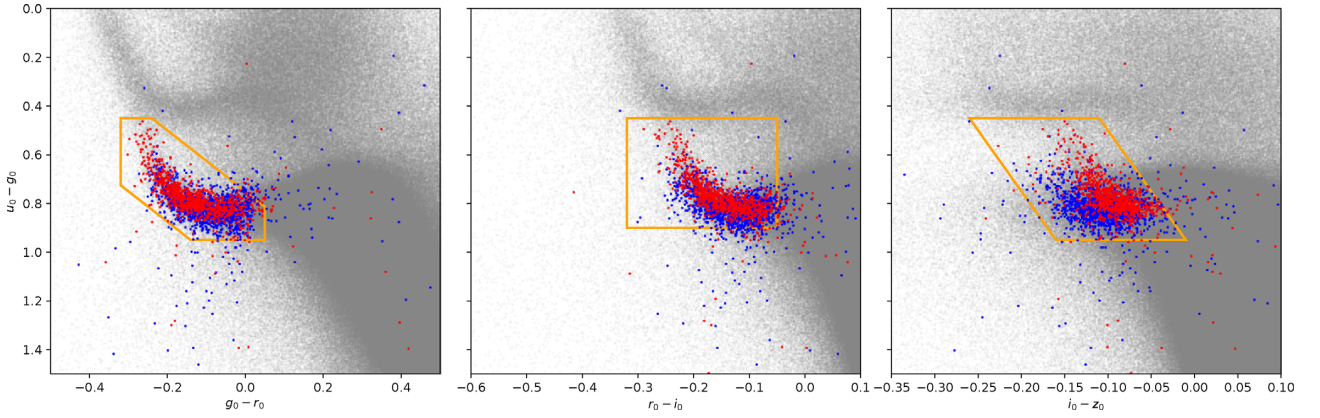


Figure 2. Stellar colour–colour diagram where the grey dots are point sources in the CFIS-PS1 data and the red and blue dots are, respectively, the BHB and BS samples of Xue et al. (2011). The orange boxes show the different colour cuts that we use to select A-type stars.

In what follows, we used the spectroscopic sample of A-stars from Xue et al. (2011), mostly composed of BHB and BS, crossmatched to CFIS, as the training set for the Principal Component Analysis (PCA) described below.

3 THE CFIS BHB STARS

3.1 Selection of BHB stars

BHBs are hot, A-type stars ($7500 \lesssim T_{\text{eff}} \lesssim 9000$ K). A-type stars can be easily identified and separated from others types of stars with colour–colour cuts involving the u band (Yanny et al. 2000; Sirko et al. 2004; Deason et al. 2011). However, we note that using only the $(g_0 - r_0)$ versus $(u_0 - g_0)$ colour–colour diagram to select A-stars (Sirko et al. 2004; Deason et al. 2011), results in significant contamination from cooler stars.

We select A-type stars using three different colour–colour diagrams [$(g_0 - r_0)$ versus $(u_0 - g_0)$, $(r_0 - i_0)$ versus $(u_0 - g_0)$, and $(i_0 - z_0)$ versus $(u_0 - g_0)$] as shown in Fig. 2, where the red dots are the spectroscopic BHB sample of Xue et al. (2011). It is important to note that the $(u_0 - g_0)$ colour of our catalogue is shifted by $\simeq 0.3$ mag compared to the same colour using the SDSS u and g filters, since the filters are not the same. Applying these selections on the 9.2×10^7 sources of the crossmatched CFIS-PS1 catalogue leads to a sample of $\simeq 29\,700$ A-type stars.

Our simple colour cuts select both BHB and BS stars. The latter population have a higher surface gravity than BHB stars ($\log(g)_{\text{BS}} \simeq 4.2$ and $\log(g)_{\text{BHB}} \simeq 3.2$, Vickers, Grebel & Huxor 2012). This difference in surface gravity between these two populations leads to a difference in the width and the depth of surface gravity sensitive absorption lines such as the Balmer lines around 365 nm and, to a lesser extent, the Paschen lines around 870 nm. This behaviour can be used to disentangle the two populations (Sirko et al. 2004; Xue et al. 2008). Indeed, even in the absence of spectroscopic data it is possible to use photometry to discriminate between the BHB and BS. Yanny et al. (2000), Sirko et al. (2004), and Bell et al. (2010) have used the u band and its sensitivity to the Balmer jump to this end, and Lenz et al. (1998) have found that the $i - z$ colour is also sensitive to the surface gravity for A-types stars, due to the presence of the Paschen absorption lines in the z band (Vickers et al. 2012). Attempts to use the u band without the z band, or *vice-versa*, to disentangle these two populations have generally produced samples of BHB stars that are only ~ 55 per cent complete while containing

Table 1. Mean colours of the training set of A-type stars from Xue et al. (2011).

colour	(colour)
$(u_0 - g_0)$	0.7970
$(g_0 - r_0)$	−0.1138
$(r_0 - i_0)$	−0.1413
$(i_0 - z_0)$	−0.1050

up to 30 per cent contamination (Bell et al. 2010; Vickers et al. 2012).

As we can see in Fig. 2, even with these differences between the two populations, it is very difficult to discriminate between them with simple colour–colour cuts. Instead, we try to use all the information available in all the bands. To this end, we developed a discrete classification algorithm using a PCA approach based on the work of Ibata & Irwin (1997), where the inputs are the colours $(u_0 - g_0)$, $(g_0 - r_0)$, $(r_0 - i_0)$, and $(i_0 - z_0)$. We use the spectroscopic catalogue of A-type stars selected by Xue et al. (2011) as the training set to find the principal components that provide the best separation between BHB and BS stars. After crossmatching, our training set is composed of 872 BHB (39.0 per cent of the training sample) and 1366 BS (61 per cent). Following Ibata & Irwin (1997), we subtracted the mean value from each colour, since this does not contain any fundamental information and avoids the problem of the domination of the covariance matrix by the mean colour (the mean of each colour in our training set is listed in Table 1).

The principal components that provide the best separation of the two populations can be found by this algorithm and is described by the following equation, where P_1 is the principal component corresponding to the highest eigenvalue of the covariance matrix:

$$\begin{pmatrix} P_1 \\ P_2 \\ P_3 \\ P_4 \end{pmatrix} = A \cdot \begin{pmatrix} u_0 - g_0 \\ g_0 - r_0 \\ r_0 - i_0 \\ i_0 - z_0 \end{pmatrix}, \quad (2)$$

where

$$A = \begin{pmatrix} -0.6397 & -0.7669 & 0.0493 & -0.0149 \\ -0.6479 & 0.5353 & -0.2283 & -0.4916 \\ -0.3964 & 0.3141 & 0.0040 & 0.8626 \\ -0.1181 & 0.1633 & 0.9723 & -0.1183 \end{pmatrix}. \quad (3)$$

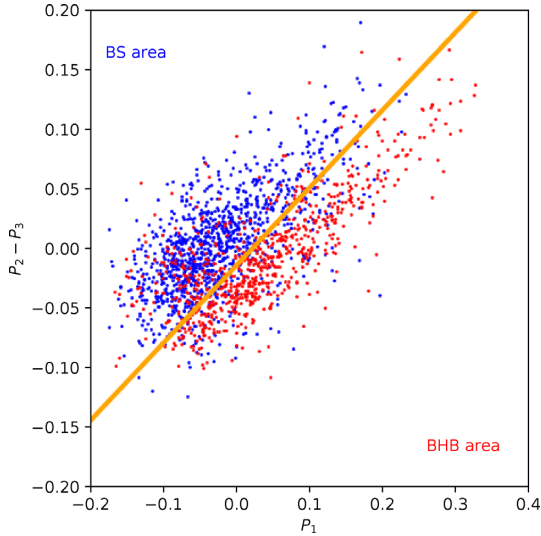


Figure 3. Separation of the BHB and BS area with the two axes determined by the PCA analysis. The red and blue dots correspond, respectively, to BHB and BS from the catalogue of Xue et al. (2011).

We find that the minor axis (P_4) does not help to disentangle the two populations. This is unsurprising, since we can see that the P_4 axis is mostly influenced by $(r_0 - i_0)$, a colour that does not contain hydrogen lines sensitive to the surface gravity that can help to separate the two populations (and which does not play an important role in the construction of the three other axes). Our findings are in line with the idea of Lenz et al. (1998) that the BHB and the BS are separated efficiently using the Balmer and Paschen lines present in the u , g , i , and z bands. In what follows, we just use P_1 , P_2 , and P_3 to separate the BHB from the BS stars.

Using these three axes, it is possible to define a region mostly populated by the BHB stars, as seen in Fig. 3, such that:

$$(P_2 - P_3)_{\text{BHB}} \leq -0.0141 + 0.6512 P_1. \quad (4)$$

Using this definition, we can define a photometric sample of BHB that contains 71 per cent of the overall BHB sample of the training set, with a contamination from the BS in the training set that is only 24 per cent of the photometric BHB sample. In order to account for the photometric uncertainties in each band, we have resampled the input colours of the training set 100 times accounting for their measurement errors and we found that, even with the photometric uncertainties, the completeness of the photometric BHB did not change and that the contamination never increased to larger than 26 per cent of this sample.

Seven globular clusters fall within the current CFIS footprint, NGC 2419, NGC 5272, NGC 5466, NGC 6205, NGC 6341, Palomar 4, and KO 2. However, the latter does not contain any BHB stars due to its very low luminosity of $M_V \sim -1$ mag (Koposov et al. 2007), and Palomar 4 contain only two stars that we identify as A-types stars. These two clusters are not used in what follows. Using the colour–magnitude diagram (CMD) of the other five globular clusters, presented in Fig. 4, we visually selected boxes enclosing BHBs in these objects in the $0.45 \leq u_0 - g_0 \leq 0.95$ range. These selection boxes, in orange in Fig. 4, contain the stars that we consider to be bonafide BHBs, and which can be used to provide an independent test of the effectiveness of our algorithm.

The resulting completeness and purity of our photometric BHB sample as measured using these globular clusters are shown in Table 2. The completeness estimate for each globular cluster is

comparable to our earlier estimate using the spectroscopic sample of Xue et al. (2011). Our method successfully discriminates between the BHB and the BS in these globular clusters. Indeed, the purity of the BHB is > 90 per cent for all these clusters, much higher than for the spectroscopic sample. This high degree of purity is found even for NGC 5272 and NGC 5466, which have the largest populations of BS as inspection of Fig. 4 makes clear. However, the globular clusters just represent a tiny fraction of the overall population of the stellar halo and may undersample the BS population. Therefore, we adopt the more conservative contamination estimate of 24 per cent for this study. This contamination rate is similar to those found by Bell et al. (2010) and Vickers et al. (2012); however, the completeness of our sample is 1.25 higher than their corresponding BHB samples.

We calculate the P_1 and $P_2 - P_3$ axis for all of the $\simeq 29\,700$ A-types stars present in the CFIS footprint and selected a photometric sample of BHB stars using equation (4). This leads to a photometric BHB sample of $\sim 10\,200$ stars. The position of the BHB of our sample in Galactic coordinates is shown in Figure. 1.

3.2 Distances estimates

To determine the heliocentric distance of the BHB stars, we use the calibration of the absolute magnitude in the g band (M_g) provided by Deason et al. (2011), which is a function of $(g_0 - r_0)$:

$$M_g = 0.434 - 0.169(g_0 - r_0)_{\text{SDSS}} + 2.319(g_0 - r_0)_{\text{SDSS}}^2 + 20.449(g_0 - r_0)_{\text{SDSS}}^3 + 94.517(g_0 - r_0)_{\text{SDSS}}^4. \quad (5)$$

As illustrated in Fig. 5, the $(g_0 - r_0)$ colour in the Pan-STARRS 1 photometric system is slightly different from the one in the SDSS system, thus we have transformed the $(g_0 - r_0)$ colour used in the equation into the Pan-STARRS 1 photometric system by identifying a subsample of our A-types stars also identified in the SDSS data release 14. The transformation that we calculate with 1042 stars in this way is given by:

$$(g_0 - r_0)_{\text{SDSS}} = 1.18(g_0 - r_0)_{\text{PS}} + 0.02. \quad (6)$$

The typical difference between the real SDSS colour and that provided by this transformation is 0.01 mag.

Finally, we verify the accuracy of the BHB distances derived in this way by calculating the average distance of the BHBs in our sample that are spatially coincident with five known globular clusters and the Draco dwarf galaxy. These are listed in Table 3 and are consistent with the literature values for the distances to these objects.

4 EVALUATION OF THE COMPLETENESS

The most distant BHB star in our sample has a heliocentric distance of $\simeq 220$ kpc. Of course, the fraction of BHBs detected at different distances in our sample depends of the completeness of the survey. The completeness is a function of magnitude, and this in turn varies with position on the sky since, for such a large survey, the depth varies spatially and reflects the specific observational conditions at each position. In this section, we first describe the method that we used to determine the completeness of our survey in the different bands for a reference field of 1×1 deg². We then present an analysis of the spatial variation of the limiting magnitude per band.

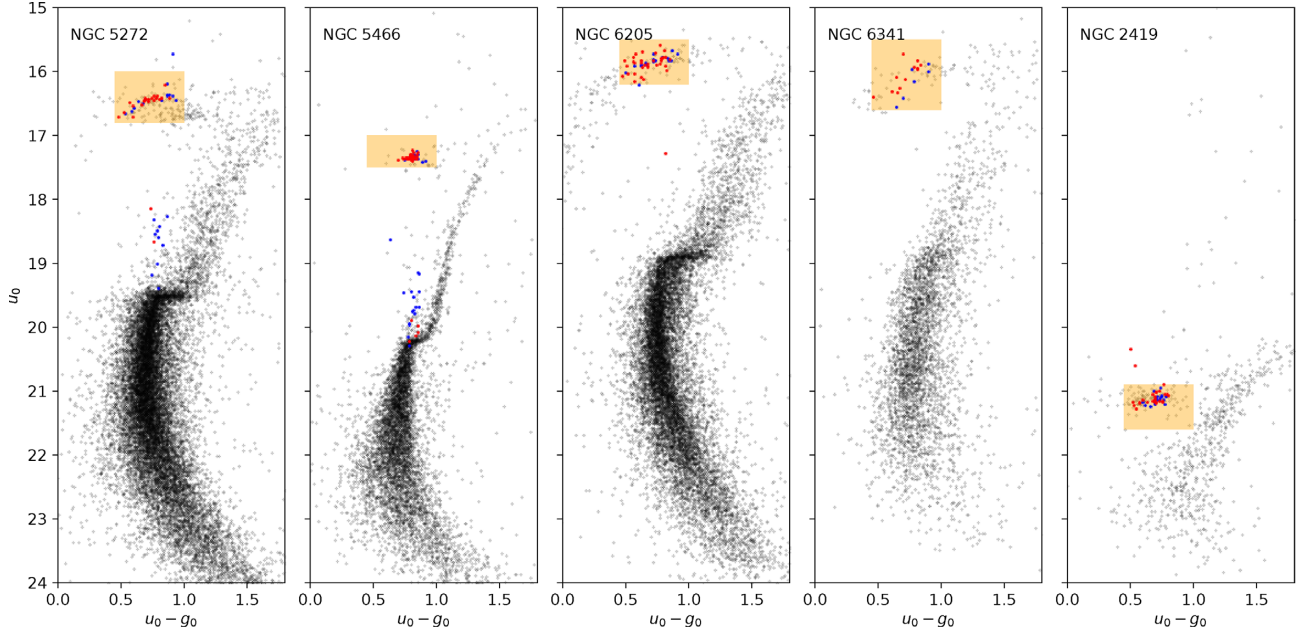


Figure 4. CMDs of five of the seven globular clusters present in the CFIS footprint where the red and blue dots correspond, respectively, to the stars identify as BHB and BS with our method. The orange area represents the region of the CMD where really lies the BHBs.

Table 2. Purity and completeness of our photometric BHB sample in five over seven globular clusters present in the CFIS footprint.

Name	Completeness	Purity
NGC 2419	0.63	0.93
NGC 5272	0.74	0.90
NGC 5466	0.64	0.92
NGC 6205	0.68	0.94
NGC 6341	0.70	1.0
Total	0.68	0.94

Table 3. Comparison of the heliocentric distance of six stellar halo objects derived using the mean magnitude of the BHB ($r_{h, \text{BHB}}$) with the previous distances to these objects derived using other tracers $r_{h, \text{past}}$.

Name	$r_{h, \text{BHB}}$ (kpc)	$r_{h, \text{past}}$ (kpc)	Source
NGC 2419	90.8 ± 7.8	$82.6^{+2.4}_{-1.4}$	Harris (1996)
NGC 5272	10.32 ± 0.76	10.2 ± 0.2	Harris (1996)
NGC 5466	16.13 ± 0.25	16.0 ± 0.4	Harris (1996)
NGC 6205	7.64 ± 0.60	7.1 ± 0.2	Harris (1996)
NGC 6341	8.58 ± 0.68	8.3 ± 0.2	Harris (1996)
Draco dSph	82.0 ± 4.5	79.79 ± 2.31	Sesar et al. (2017)

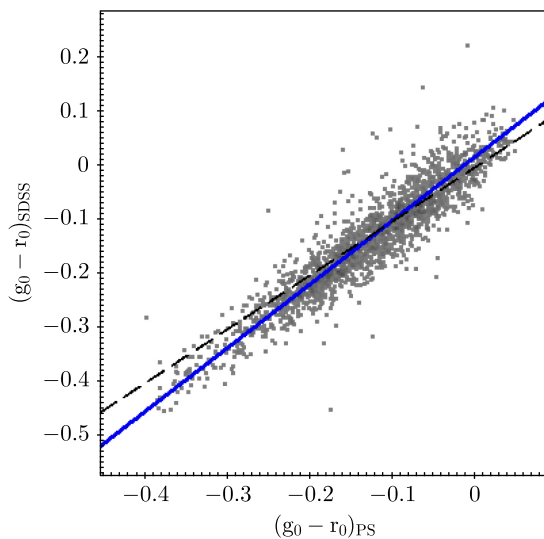


Figure 5. Relationship between the $(g_0 - r_0)$ colour using the PS1 and the SDSS filters system. The dashed line shows the relation if $(g_0 - r_0)_{\text{SDSS}} = (g_0 - r_0)_{\text{PS}}$, and the blue line shows the best-fitting linear relation described in equation (6).

4.1 The completeness of the reference field

The band that has the most influence on the completeness of our sample is not the u band since it is considerably deeper than the PS1 data [$\text{SNR} = 5$ at $u \sim 24.5$ (Ibata et al. 2017)]. All the other bands are shallower by at least ~ 1 mag. The maximum difference of the magnitude between the u and the others bands for A-types stars is less than 1 mag. Therefore, the completeness of our BHB sample is set by the completeness of PS1.

We estimate the completeness of our sample by comparing the number of sources detected as a function of magnitude to a considerably deeper field in similar bandpasses. To this end, we define a reference field of 1×1 degree taken from the area covered by the recent data release 1 of the Hyper Suprime-Cam Subaru Strategic Program (hereafter HSC-SSP, Aihara et al. 2018), which is significantly deeper than PS1. Unfortunately, at the time of our study, there is no region that is covered by both the HSC-SSP and CFIS. However, as mentioned before, the completeness of our BHB sample depends primarily on the completeness of PS1, which has full coverage of all the sky visible from Hawaii. Our reference field is centred at R.A. = 245.5 deg and Dec. = 43.5 deg, close to the CFIS footprint and in the HSC footprint.

We selected only objects with uncertainties < 0.2 dex in the g , r , i , and z bands of the two catalogues and applied the criterion defined

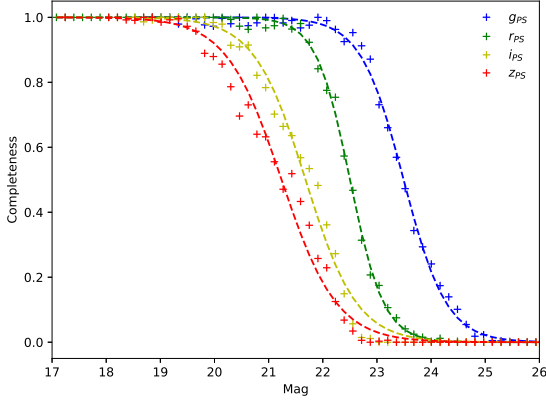


Figure 6. Completeness of the g , r , i , and z bands of the PS1 survey in an area of 1 deg^2 centred at (R.A., Dec.) = (245.5, 43.5), assuming that all stars brighter than 26 mag are present in the HSC-SSP survey.

Table 4. Parameters of the fit of the completeness of $griz$ bands of PS1 used in equation (8).

Band	a	b
g	23.54	0.4
r	22.55	0.31
i	21.74	0.48
z	21.24	0.51

in equation (1) on the PS1 data to select only the objects that we identify as stars. We crossmatch the catalogues and calculate the fraction of HSC stars¹ that are also identified in PS1. The resulting completeness curves for each band are shown in Fig. 6, where we have used the following equations to transform the HSC filter system to the PS1 filter system where k_{RMS} is the mean difference between the PS magnitude determined by this equation and the real PS magnitude in the k band :

$$\begin{aligned}
 g_{\text{PS}} &= 1.005 g_{\text{HSC}} - 0.00025 g_{\text{HSC}}^2 & g_{\text{RMS}} &= 0.2 \\
 r_{\text{PS}} &= r_{\text{HSC}} + 0.034 & r_{\text{RMS}} &= 0.11 \\
 i_{\text{PS}} &= i_{\text{HSC}} + 0.1 & i_{\text{RMS}} &= 0.08 \\
 z_{\text{PS}} &= z_{\text{HSC}} + 0.1 & z_{\text{RMS}} &= 0.04.
 \end{aligned} \tag{7}$$

Although g_{RMS} is large, this imprecision will not have an impact on our study, as the g band is not the band that limits the completeness of our BHB sample (see below).

We find that the data in Fig. 6 can be reasonably fit with the following generic exponential equation, where C_x is the completeness in one band:

$$C_x = 1.0 / (1.0 + \exp((x - a)/b)). \tag{8}$$

The parameters a and b for each band are listed Table 4.

In Fig. 6, it is clear that the z band is the shallowest band, with a 50 per cent of completeness that is 0.45 mag shallower than for the i band. Moreover, more than 98 per cent of our sample of A-types stars have a non-reddened colour $|i - z| < 0.2$. Thus we conclude that the completeness of our BHB sample is primarily determined by the completeness of the z band. Therefore, we use the equation of completeness in the z band in our subsequent analysis

¹We defined the stars in the HSC data set such as $iclassification_{\text{extendedness}} = 0$.

to account for completeness effects due to the magnitude limits of the survey (see Section 5). We also note that our reliance on the PS1 data means that we are not yet fully exploiting the depth of the CFIS data, and that we can expect to conduct even deeper studies in the future once deeper z -band data become available.

4.2 Spatial variation of the completeness

The HSC-SSP survey covers only a tiny fraction of PS1, and it is impossible to do a similar analysis on the full PS1 footprint to study the spatial variation of the completeness directly. Nevertheless, it is possible to study the variation in the relative depth of the survey, and so relate this back to the completeness of the reference field, through the luminosity function of each band at a given position.

We allow for the fact that the variation in the depth of PS1 may be extremely complex because of the survey strategy, range of observing conditions, and multiple observations of the same region. Therefore, we cut the PS1 survey into ‘pixels’ of 1×1 degrees in right ascension and declination, and calculate the luminosity function per pixel in each of the g , r , i , and z bands. Due to spherical geometry, the number of stars per pixel in the highest declination regions is significantly lower than close to the equatorial plane. However, our survey is currently limited to $\delta \leq 60$ degrees, and this issue has a negligible impact on the following analysis (the variation of the number of stars per pixel at high declinations is still lower than the Poissonian uncertainty of the most populated pixel).

We define the ‘limiting magnitude’ of each pixel in a given band as the magnitude where the luminosity function, normalized to the maximum value in each pixel, is equal to 0.5. The variation of the limiting magnitude of each pixel of the z band of the PS1 survey over the CFIS footprint is shown in Fig. 7. The limiting magnitude of the reference field used above to determine the completeness of PS1 is $z_{\text{lim,ref}} = 22.09$. The mean limiting magnitude over the full CFIS footprint in the z band is of $\langle z_{\text{lim}} \rangle = 22.06$ with a standard deviation of $\sigma_{z_{\text{lim}}} = 0.01$ mag.

We then approximate the completeness of a pixel centred on (R.A., Dec.) = (α, δ) in the z band using equation (8) where z is replaced by $z'(\alpha, \delta)$, defined so that:

$$z'(\alpha, \delta) = z - (z_{\text{lim}}(\alpha, \delta) - z_{\text{lim,ref}}). \tag{9}$$

We verify that this approximation is valid by comparing the completeness determined in this way with the completeness measured directly (using the technique in the previous section) on a different field covered by the HSC-SSP and PS1. Fig. 8 shows this comparison for the z band on a field centred at (R.A., Dec.) = (132.5, 52.5). It is clear from this figure that this method reproduces very well the completeness of that field: the difference in the z value used to define the two curves in only 0.02 mag.

5 THE SMOOTH STELLAR HALO PROFILE

In this section, we lay out how we construct a model of the smooth stellar halo traced by our photometric BHB sample, accounting for the observational biases such as the completeness of the sample defined in the previous section. The following analysis is similar to the study done recently with the RR Lyrae of PS1 by Hernitschek et al. (2018). However, our selection function, that introduces the observational biases in our model, is slightly different, since the spatial footprint of the surveys and the stellar populations used are different. This kind of approach has been employed by Bovy et al. (2012) and Rix & Bovy (2013) for the disc of the Milky Way and by Ibata et al. (2014) for the stellar halo of the Andromeda galaxy.

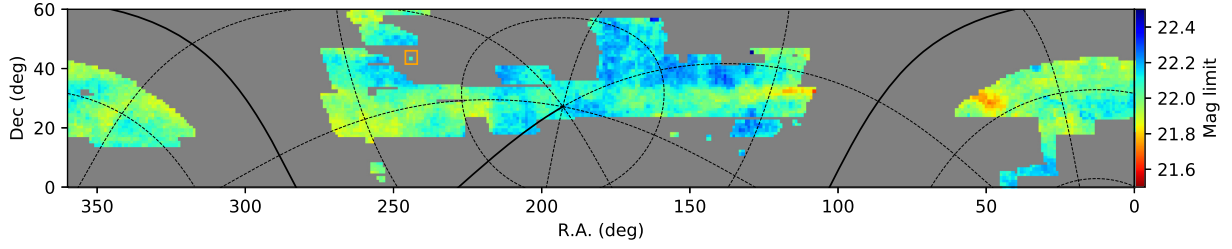


Figure 7. Map of the spatial variation of the limiting magnitude in the z band over the CFIS footprint. The orange square highlights the reference field used to determine the completeness. The black lines show Galactic coordinates, with the Galactic plane and Galactic minor axis highlighted with a solid line.

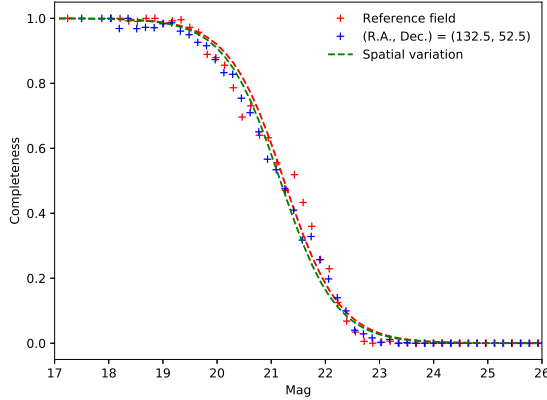


Figure 8. The completeness of the z band of our primary reference field (R.A., Dec.) = (245.5, 43.5) is shown in red. The completeness of another field, centred on (R.A., Dec.) = (132.5, 52.5), is shown in blue, where we have calculated the completeness by direct comparison to HSC data, in the same way as the primary field. The red dashed line is for these points. The green dashed line shows the predicted completeness of this field using equation (9) and the method outlined in the text. The two methods agree very well.

In the following, (X, Y, Z) are the Galactic Cartesian coordinates,² $R_{GC} = \sqrt{X^2 + Y^2 + Z^2}$ is the Galactocentric radius, r_{helio} is the heliocentric distance, and $m = \sqrt{X^2 + Y^2 + (Z/q)^2}$ is the elliptical distance that allow a vertical deformation of the stellar halo compared to the plane of the Galactic disc through the parameter q , such that the stellar halo is spherical if $q = 1$, oblate if $q < 1$, and prolate if $q > 1$. In this work, we assumed that the Sun is located in the plane of the disc ($Z_{\odot} = 0.0$ kpc) at a distance from the Galactic centre of $R_{\odot} = 8.5$ kpc. The Cartesian Galactocentric coordinates of the BHB stars are shown in Fig. 9.

5.1 Stellar distribution model

It is common to model the spatial distribution of a single stellar population of the outer stellar halo ($R_{GC} > 15$ kpc) by an axisymmetric distribution following a single or a broken double power law, depending of the complexity of the model. As we will soon see, a single power law is sufficient to provide an adequate description of the spatial distribution of our BHB sample. The generic form of this profile is given by:

$$\rho(m) = \rho_{\odot} (R_{\odot}/m)^{\gamma}, \quad (10)$$

²In this work, we used the right-hand coordinates, with the x -axis pointing toward the Sun and the z -axis toward the North galactic pole.

where γ is the slope of the power law and ρ_{\odot} is the density of stars at the Solar radius (R_{\odot}). As we are interested only in the shape of the profile of the stellar halo traced by the BHB and not on the total number of BHB, ρ_0 is fixed to 1 in our model.

Some recent studies favour a broken power law to model the smooth profile of the halo (e.g. Watkins et al. 2009; Deason et al. 2014; Xue et al. 2015), with a break radius around or below 20 kpc. To compare our result with these previous studies, we also implement a broken power-law profile. The generic form is given by:

$$\rho(m) = \rho_{\odot} \begin{cases} (R_{\odot}/m)^{\gamma} & \text{for } m \leq r_b \\ (R_{\odot}/r_b)^{\gamma-\beta} (R_{\odot}/m)^{\beta} & \text{for } m > r_b \end{cases}, \quad (11)$$

where γ and β are the inner and outer slope, respectively, and r_b is the break radius (the radius where the change of the slope occurs).

In these models, we assume that the flattening is constant and independent of the Galactocentric radius. However, as pointed out by Preston, Shectman & Beers (1991) using both BHB and RR Lyrae, the flattening of the stellar halo may vary with distance (they find that the flattening decreases with Galactocentric radius). This result has been confirmed by Carollo et al. (2007) and Schönrich, Asplund & Casagrande (2011), who identify two structural components to the stellar halo: the inner halo, that they argue is formed by *in situ* stars and has an oblateness $q \sim 0.6$ and the outer halo that they argue is formed via accreted stars, which is more spherical with an oblateness of $q = 0.9-1.0$. Following Hernitschek et al. (2018), we implemented a variation of the flattening of the halo as a function of Galactocentric distance (R_{GC}) for the single power-law profile such that:

$$q(R_{GC}) = q_{\infty} - (q_{\infty} - q_0) \exp\left(1 - \frac{\sqrt{R_{GC}^2 + r_q^2}}{r_q}\right), \quad (12)$$

where q_0 is the flattening at the centre of the halo, and q_{∞} is the flattening at large galactocentric distance. r_q is a characteristic radius marking a change between these values.

We did not implement a triaxial model since, as illustrated in Figure. 1, a great fraction of the northern Galactic hemisphere is not observed by CFIS at the present time.

5.2 Construction of the selection function

A good estimate of the selection function is mandatory to account for the observational biases that can affect our estimate of the real shape of the stellar halo, such as the completeness of the BHB sample or the spatial footprint of the survey. We separate our selection function in different categories to take into account these different effects.

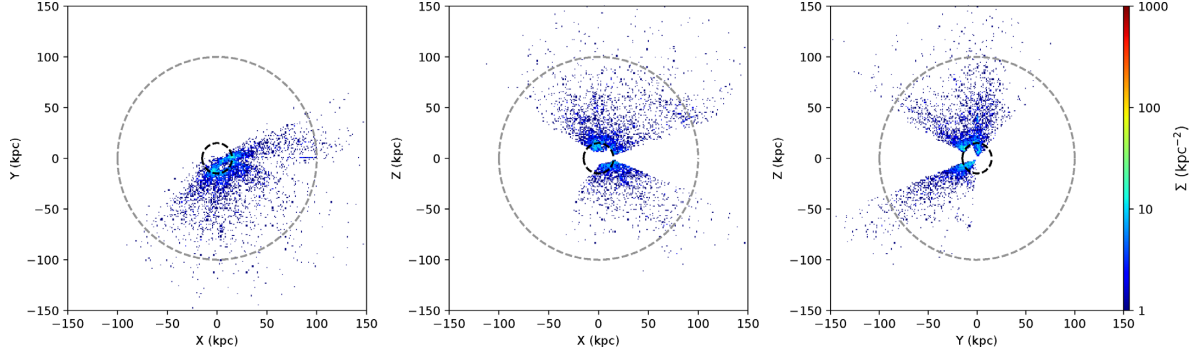


Figure 9. Galactocentric coordinates of the BHB stars. The dark circle corresponds to a radius of 15 kpc and the grey circle to a radius of 100 kpc.

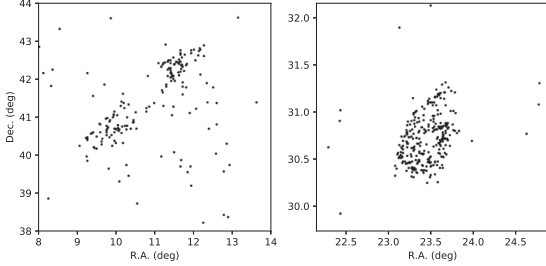


Figure 10. Point sources incorrectly identified as BHB stars around the Andromeda (left-hand panel) and the Triangulum (right-hand panel) galaxies.

First, the CFIS footprint leads us to use in our analysis only the region covered by the survey, such that :

$$S_{\text{area}}(l, b) = \begin{cases} 1 & \text{if } (l, b) \text{ in CFIS} \\ 0 & \text{otherwise} \end{cases} \quad (13)$$

Our study is focused on the profile of the outer stellar halo (>15 kpc), and so we only use stars that we estimate lie at a Galactocentric distance between 15 and 220 kpc (corresponding to the distance of the farthest BHB in our sample), as described by :

$$S_{\text{outer halo}}(R_{\text{GC}}) = \begin{cases} 1 & \text{if } 15 < R_{\text{GC}} < 220 \text{ kpc} \\ 0 & \text{otherwise} \end{cases} \quad (14)$$

We notice that some point sources, identified as BHB stars by our algorithm, are in the vicinity of the two clusters in the Andromeda (M 31) and Triangulum (M33) galaxies, and trace the shape of these galaxies (see Fig. 10). At the distance of M 31, 778 ± 19 kpc (Conn et al. 2011, 2012), a typical BHB star should have an apparent magnitude of $z = 24.95$, much fainter than the detection limit of the PS1 data. Thus, these point sources are probably young (<10 Myr) main sequence stars or even star clusters, which have an absolute magnitude of $M_g \sim -5$ (Davidge et al. 2012). Two known galactic objects, Draco, NGC 2419 and NGC 5466, are also present in the range $15 < R_{\text{GC}} < 220$ kpc in the CFIS footprint, and their presence would impact the determination of the radial profile of the smooth halo. Thus we remove five regions around M 31, M 33, NGC 2419, NGC 5466, and Draco through the selection function so that:

$$S_{\text{conta}}(l, b) = \begin{cases} 0 & \text{if } d_{M31} < 4.0 \text{ deg} \\ 0 & \text{if } d_{M33} < 2.0 \text{ deg} \\ 0 & \text{if } d_{\text{NGC } 2419} < 0.4 \text{ deg} \\ 0 & \text{if } d_{\text{NGC } 5466} < 0.4 \text{ deg} \\ 0 & \text{if } d_{\text{Draco}} < 0.5 \text{ deg} \\ 1 & \text{otherwise} \end{cases} \quad (15)$$

where d_{M31} , d_{M33} , $d_{\text{NGC } 2419}$, $d_{\text{NGC } 5466}$, and d_{Draco} are the angular separation of stars relative to the centres of M 31, M 33, NGC 2419, NGC 5466, and Draco, respectively.

As pointed out by Deason et al. (2011), substructures – and particularly the Sagittarius stream (Sgr stream) – could affect the determination of the slope of the smooth halo profile. A significant portion of our survey contains the Sgr stream ($\sim 1/5$), and it is important to account for it. We prefer to remove all stars in the footprint that fall within 10 deg (Majewski et al. 2003) of the main Sgr stream orbit, rather than removing only the stars that have a good probability to be part of the stream using their distances. The latter method is dependent on a model of the variation of the distance to the stream that is usually assumed to match the simulation of Law & Majewski (2010) (although this does not reproduce the distance of the farthest arm of the stream, Belokurov et al. 2014; Thomas et al. 2017). The selection function we implement is thus given by :

$$S_{\text{Sgr}}(l, b) = \begin{cases} 0 & \text{if } |\tilde{B}| < 10.0 \text{ deg} \\ 1 & \text{otherwise} \end{cases} \quad (16)$$

where \tilde{B} is the longitude of the Sgr stream coordinate system of Belokurov et al. (2014).

We also account for the completeness as a function of the magnitude. Here, extinction plays a role. We know the mean absolute magnitude in the z band for our photometric BHB sample is $\langle M_{z, \text{BHB}} \rangle = 0.98$, and so it is possible to calculate the mean apparent magnitude of a BHB at different distances and at different positions, so that:

$$z_{\text{BHB}}(l, b, r_{\text{helio}}) = \langle M_{z, \text{BHB}} \rangle - 5 + 5 \log(r_{\text{helio}}(1000.0/\text{kpc})) + A_z \quad (17)$$

where A_z is the Galactic foreground extinction in the z band and z_{BHB} is the mean apparent magnitude for a BHB at a distance r_{helio} .

Therefore, the selection function for the completeness of the BHB sample can be calculated from equations (8), (9), and (17) so that:

$$S_{\text{comp}}(l, b, r_{\text{helio}}) = C_z (z_{\text{BHB}} - z_{\text{lim}}(l, b) + z_{\text{lim, ref}}) \quad (18)$$

The overall selection function of our model accounting for the observations is given by:

$$\begin{aligned} \mathcal{S}(l, b, D) &= S_{\text{area}}(l, b) \times S_{\text{outer halo}}(D) \\ &\quad \times S_{\text{conta}}(l, b) \times S_{\text{Sgr}}(l, b) \\ &\quad \times S_{\text{comp}}(l, b, D), \end{aligned} \quad (19)$$

where D is distance, either r_{helio} or R_{GC} depending on the term in the equation.

5.3 Constraining the model

With the selection function \mathcal{S} , it is now possible to calculate the likelihood of the data given a set of parameters θ for each of our three models of density profile $\rho_{\text{BHB}}(\mathcal{D}|\theta)$, defined in Section 5.1, in the same way as for Hernitschek et al. (2018). The likelihood, $p_{\text{BHB}}(\mathcal{D}_i|\theta)$, of the i -th star, for a given profile of the BHB stars with the set of data \mathcal{D}_i , can be calculated as:

$$p_{\text{BHB}}(\mathcal{D}_i|\theta) = \frac{\rho_{\text{BHB}}(\mathcal{D}_i|\theta) |\mathbf{J}| \mathcal{S}(l_i, b_i, D_i)}{\int \int \int \rho_{\text{BHB}}(l, b, D|\theta) |\mathbf{J}| \mathcal{S}(l, b, D) dl db dD}. \quad (20)$$

The denominator of this equation is the normalization factor, where the integral is over the observed volume. As pointed out by Hernitschek et al. (2018), the Jacobian term $|\mathbf{J}| = D^2 \cos b$ is required to transform from the Cartesian to Galactic coordinates.

As mentioned in Section 3, we estimate that up to 24 per cent of our photometric BHB sample may be contaminated from other A-types stars, mostly composed of BS. At a given distance, the BS population is less luminous than the BHB ($M_{g, \text{BS}} \simeq 2.5$ and $M_{g, \text{BHB}} \simeq 0.7$, Deason et al. 2011). By misidentifying BS as BHB, we can potentially modify the derived profile, particularly at large radius since we will misidentify faint BS in the disc as bright BHB in the distant halo. To account for this contamination, we define the unmarginalized likelihood $p(\mathcal{D}_i|\theta)$ of the i -th star as:

$$p(\mathcal{D}_i|\theta, \theta_{\text{conta}}) = (1 - \alpha) p_{\text{BHB}}(\mathcal{D}_i|\theta) + \alpha p_{\text{conta}}(\mathcal{D}_i|\theta_{\text{conta}}), \quad (21)$$

for a given BHB profile defined by the set of parameters θ and a contamination profile defined by the parameter set θ_{conta} . α is the fraction of the sample due to contaminant stars, fixed at $\alpha = 0.24$. $p_{\text{conta}}(\mathcal{D}_i|\theta_{\text{conta}})$ is the likelihood of the i -th star for a given contamination profile. This last term can be calculated with the same method used to calculate $p_{\text{BHB}}(\mathcal{D}_i|\theta)$ described by equation (20), replacing $\rho_{\text{BHB}}(l, b, D|\theta)$ by $\rho_{\text{conta}}(l, b, D|\theta_{\text{conta}})$. The determination of the density distribution of the contaminant stars is detailed in Section 6.1.

The posterior probability of the set of parameters θ is equal to $\ln p(\theta, \theta_{\text{conta}}|\mathcal{D}) = \sum_i \ln p(\mathcal{D}_i|\theta, \theta_{\text{conta}}) + p(\theta)$, where $p(\theta)$ is the uniform flat prior of the set of parameters.

For the single power-law profile with a constant oblateness, the parameters are defined over the following ranges:

$$\begin{aligned} 1.0 &\leq \gamma \leq 6.0 \\ 0.1 &\leq q \leq 2.0, \end{aligned} \quad (22)$$

For the single power-law profile with $q(R_{\text{GC}})$, the parameters are defined over the following ranges:

$$\begin{aligned} 1.0 &\leq \gamma \leq 6.0 \\ 15.0 &\leq r_q(\text{kpc}) \leq 220.0 \\ 0.1 &\leq q_0 \leq 2.0 \\ 0.1 &\leq q_\infty \leq 2.0. \end{aligned} \quad (23)$$

Finally, for the broken power-law profile, the parameters are defined over the following ranges:

$$\begin{aligned} 1.0 &\leq \gamma \leq 6.0 \\ 1.0 &\leq \beta \leq 6.0 \\ 15.0 &\leq r_q(\text{kpc}) \leq 220.0 \\ 0.1 &\leq q \leq 2.0. \end{aligned} \quad (24)$$

To find the set of parameters that best match our data, we explore the parameter space with the Goodman & Weare's Affine Invariant Markov Chain Monte Carlo (Goodman & Weare 2010) implemented by Foreman-Mackey et al. (2013) in the PYTHON module

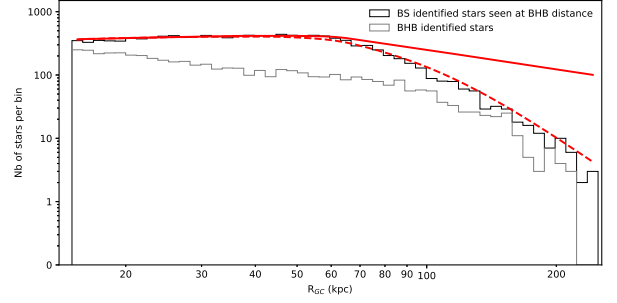


Figure 11. Comparison of the profile of the stars identified as BHB (in grey) with the profile of the stars identified as BS at the distance as if they were identified as BHB (in black). The solid red line and dashed red line shows the preferred broken power-law fit to this profile as described in the text, with and without the selection effects, respectively.

emcee. It is worth noting that from the initial $\simeq 10\,200$ BHB stars in our sample, only $\simeq 5900$ are in the outer stellar halo ($R_{\text{GC}} > 15$ kpc). Of these, $\simeq 1100$ are in the Sgr regions. Thus, our study of the profile of the outer stellar halo is done using a sample of $\simeq 4800$ BHB.

6 RESULTS AND DISCUSSION

6.1 The effect of the blue straggler contamination

To estimate the density distribution of contaminants, we assume that the normalized profile of the contamination is similar to the normalized profile of the stars that we identified as BS (Section 3), with distances derived under the assumption that they are BHB. We refer to these stars as *misidentified BS*. Fig. 11 shows that the profile of the BHB (assuming no contamination, black line) and the misidentified BS (grey line) have very different shapes. The number of BHB decreases rapidly after 100 kpc, due to the completeness of the sample. However, the number of BS decreases rapidly at a shorter distance, ~ 70 kpc. This is because most BS are located at much closer intrinsic distances (in the disc of the Galaxy), compared to the BHB that are mostly in the halo.

We choose to model the density distribution of the misidentified BS by a broken power law. We use the method described previously (with $\alpha = 1$). The fitted profile is shown in Fig. 11 as a dashed red line (no selection effects) and as a solid red line (selection effects incorporated). As visible in Fig. 12, the double broken power-law profile has an inner slope $\gamma = 2.95 \pm 0.03$, an outer slope $\beta = 4.03 \pm 0.06$, a break radius $r_b = 73.7^{+2.9}_{-2.6}$ kpc, and a flattening of $q = 0.58 \pm 0.01$. We used this profile in equation (20) and (21) to model the distribution of the contaminant stars present in our BHB sample, as described in the previous section.

6.2 Results of the Markov Chain Monte Carlo

We apply the method described Section 5.1 on our BHB sample with the three density distributions mentioned previously. As illustrated by Fig. 13, in the case of the single power law with a constant flattening, the distribution of BHB stars is best reproduced with a slope of $\gamma = 3.73^{+0.03}_{-0.02}$ and a constant flattening of $q = 0.86 \pm 0.02$. The best-fitting parameters of the broken power-law density profile has an inner slope $\gamma = 4.24 \pm 0.08$, an outer slope $\beta = 3.21 \pm 0.07$, a break radius of $r_b = 41.4^{+2.5}_{-2.4}$ kpc, and a flattening $q = 0.86 \pm 0.02$ (Fig. 14). This is similar to the flattening found with the single

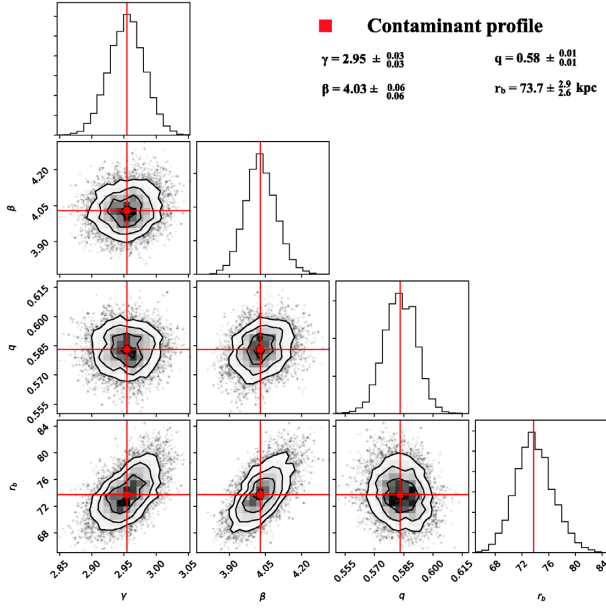


Figure 12. One-dimensional and two-dimensional posterior distribution function of the parameters used to model the contamination distribution, assuming that the contamination follow a broken power law.

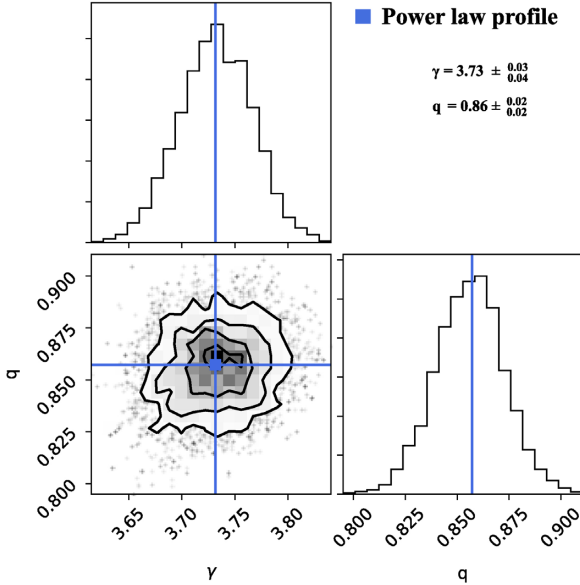


Figure 13. One-dimensional and two-dimensional posterior distribution function of the parameters used in the single power-law model with a constant flattening.

power law. Finally, Fig. 15 shows the best-fitting parameters for the single power-law model with a variation in the flattening as a function of radius. This model favours a steeper slope of $\gamma = 3.89^{+0.06}_{-0.05}$ compared to model with a constant flattening. Furthermore, this model has an oblate central region with an inner flattening of $q_0 = 0.82 \pm 0.02$, a prolate shape in its outskirts with an outer flattening of $q_{\text{infty}} = 1.39^{+0.31}_{-0.19}$ and a transition radius of $r_q = 119.9^{+48.0}_{-34.6}$ kpc. As shown by the inset panel in Fig. 15, this results in a halo that is oblate until 70–200 kpc and prolate after this radius. The large uncertainties on the shape is mostly a consequence of the low precision with which we can measure the transition radius.

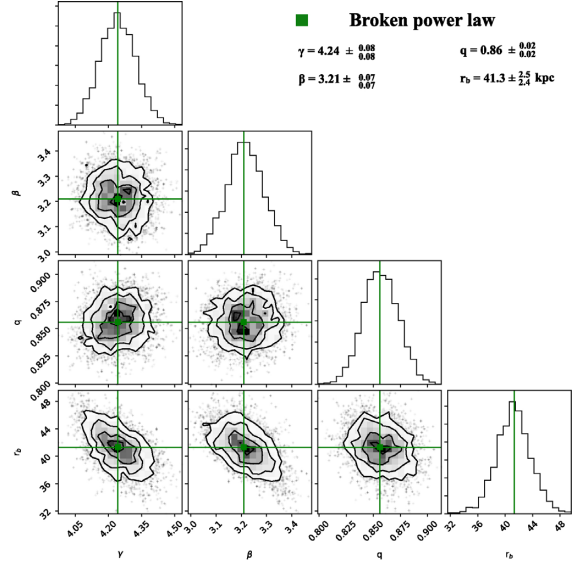


Figure 14. One-dimensional and two-dimensional posterior distribution function of the parameters used in the broken power-law model.

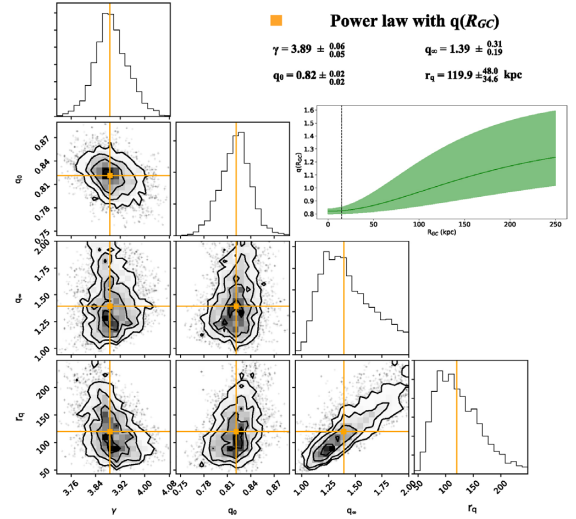


Figure 15. One-dimensional and two-dimensional posterior distribution function of the parameters used in the single power-law model with a varying flattening.

The best-fitting versions of the distribution of BHB stars for each of these model are shown by the light blue, green, and orange lines in Fig. 16 (single power law, broken power law, variable flattening, respectively). The dashed red line shows the expected contamination from BS stars as discussed earlier. The observed radial profile of BHB stars is shown by the black histogram, and the grey histogram shows the total distribution of the BHB including the region covered by the Sgr stream, where a clear overdensity can be seen in the range $70 < R_{\text{GC}} < 90$ kpc, in agreement with the distance to the Sgr stream found by previous work in that region (Majewski et al. 2003; Koposov, Rix & Hogg 2010; Belokurov et al. 2014; Hernitschek et al. 2017).

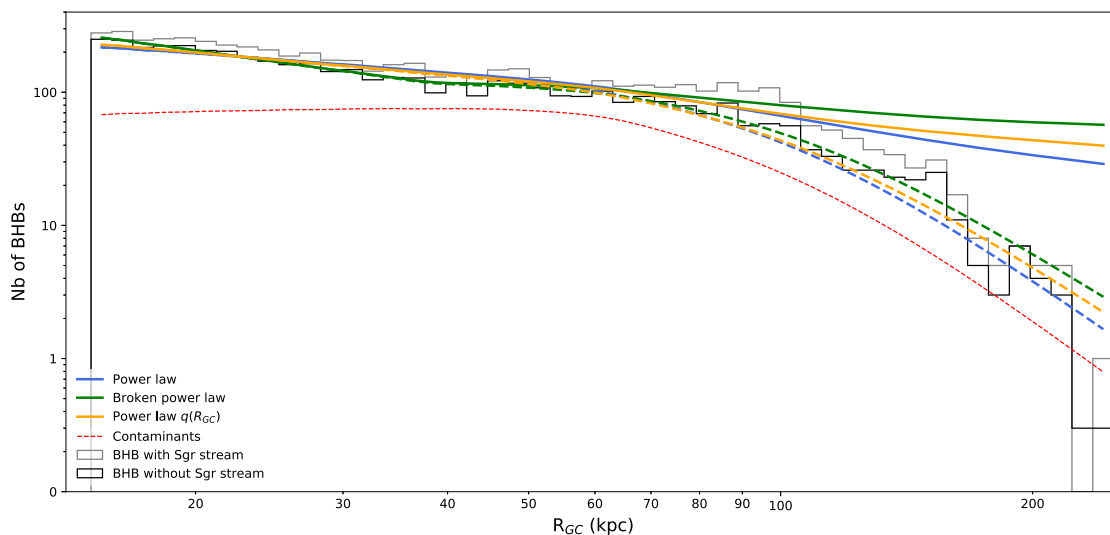


Figure 16. Number of BHB stars per distance interval. The black histogram shows our photometric BHB sample, excluding the Sgr region as described in the text. The grey histogram shows the same distribution, including the Sgr stream region. The light blue, green, and orange curves show the predicted distribution of stars for our best-fitting models using a single power-law profile, the broken power-law profile, and the single power law with a varying flattening, respectively. The dashed lines show the same functions incorporating the observational biases encoded in the selection function. The expected contamination from BS is shown by the dashed red lines.

Table 5. Table of the BIC for each of our models. ΔBIC refer to the difference between the BIC of a given model to the favourite model (with the lower BIC).

Model	$\ln p(\mathcal{D} \theta)_{\max}$	BIC	ΔBIC
Power law	-23046	46109	58
Broken power law	-23008	46051	0
Power law $q(R_{GC})$	-23421	46877	826

6.3 Preferred models

To know which of our different models is statistically preferred, given the different number of parameters in each, we use the Bayesian information criterion (BIC). This is defined as:

$$\text{BIC} = \text{dim}(\theta) \ln(N) - 2 \ln p(\mathcal{D}|\theta)_{\max}, \quad (25)$$

where N is the number of BHB stars in our sample (~ 4800) and $\text{dim}(\theta)$ is the number of dimension of θ , such that $\text{dim}(\theta) = 2$ for the single power-law profile with a constant flattening and $\text{dim}(\theta) = 4$ for the other two models.

The different values of the BIC for the three models used in our study are given in Table 5. The broken power law is formally preferred, since a model with $\Delta\text{BIC} > 10$ indicates strong evidence against this model (Kass & Raftery 1995). Both models that adopt a constant flattening are strongly preferred over the model with variable flattening.

6.4 Comparison to the literature

Our analysis favours a broken power-law profile, with an inner slope that is steeper than in the outskirts of the halo, with a transition around 40 kpc. The difference between the slope in the outer and inner region is ~ -1 . This is similar to the difference found by Hernitschek et al. (2018) with the RR Lyrae from PS1, and these authors also found a break radius around 40 kpc. However, their analysis favours a single power-law profile and the absolute values

of their inner and outer slope are much steeper than the slope found using the CFIS BHB stars.

The inner slope ($\gamma = 4.24 \pm 0.08$) is close to the recent measure of 4.5 ± 0.3 between 11.8 and 20 kpc done by Wan et al. (2018) using BHB from SkyMapper. Our measurement is also similar to the slope of 4.5 found by Watkins et al. (2009) and to the single power-law profile of Hernitschek et al. (2018) with a slope of $4.40^{+0.05}_{-0.04}$ with RR Lyrae. Moreover, our inner slope is in agreement with the slope of $\gamma = 4.5$ found by Deason et al. (2014) using BHB stars in the SDSS between 25 and 65 kpc. However, Deason et al. (2014) find a very steep slope of 6–10 at large distances. We postulate that this very steep slope is possibly a consequence of an incorrect estimate of the completeness of their BHB sample. For example, we can see in Fig. 16 that the observed profile of the BHB sample is much steeper after ~ 90 kpc, but this change in slope is fully accounted for by the completeness correction. After the break radius located at $r_b = 41.4^{+2.5}_{-2.4}$, the BHB profile is shallower and has an outer slope of $\beta = 3.21 \pm 0.07$. This is consistent with the slope of 3.2 found by Fukushima et al. (2018) between 50 and 210 kpc but is more shallow than the slope found by Watkins et al. (2009), Cohen et al. (2017), and Hernitschek et al. (2018) after 50 kpc with the RR Lyrae. All these profiles are much steeper than the value of $\gamma = 2.5$ found by De Propris et al. (2010) with the Two-Degree Field Quasar Redshift Survey; the slope of this profile is more than 30σ away from our measurement.

Other tracers have also been used to trace the profile of the outer stellar halo and these are summarized in Fig. 17. Bell et al. (2008) show that the profile of the stellar halo can be described by a power-law slope of 2–4 based on a sample of over 4 million main sequence turn-off stars out to 40 kpc. Pila-Díez et al. (2015), using F-stars and find a steep slope of 4.85 out to 60 kpc. Slater et al. (2016), using a sample of photometrically selected giants from DDO 51 and SDSS, find an index of 3.5 up to 80 kpc. Xue et al. (2015), using K-giants from Segue, find a power law with an index of 4.2 out to 80 kpc. We note that this last measurement is quite close to our estimate until 40 kpc. As discussed by Hernitschek et al. (2018), it is difficult to determine if this difference between tracers are

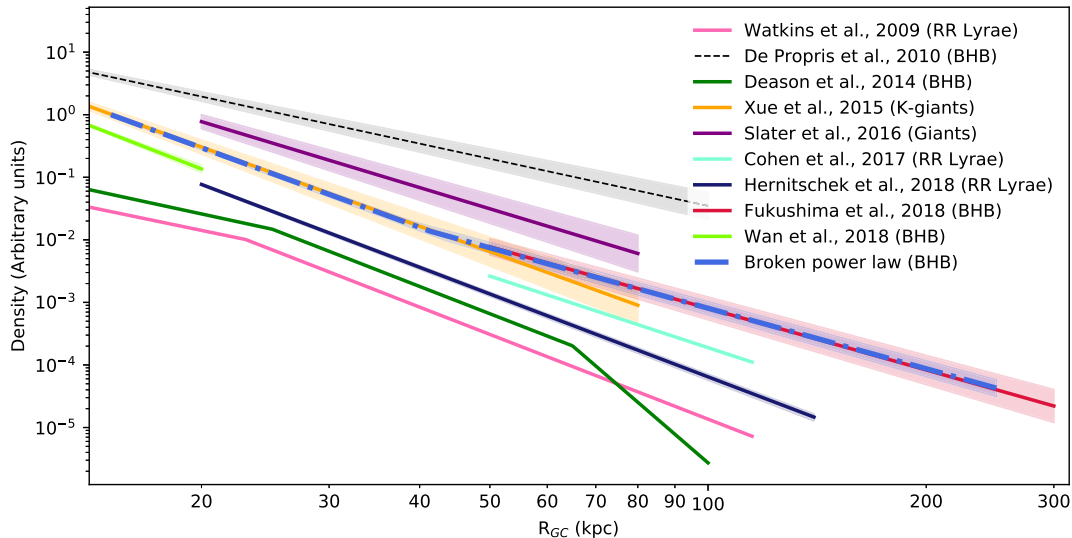


Figure 17. Comparison of our best-fitting model of the power law with a constant flattening (blue dot–dashed line) to best-fitting models of other work. The slope of the stellar halo found by De Propris et al. (2010) using BHB stars is inconsistent with the slope found by other groups, including those studies that use the same tracer population.

the consequence of intrinsic differences between the distribution of these different stellar populations, or if they are due to a difference in the methodology.

According to all these measurements, the outer stellar halo of the Milky Way is steeper than that for the Andromeda galaxy. Ibata et al. (2014) find that the three-dimensional density profile of M 31 is well reproduced by a spherical halo ($q = 1.09$) with a single power-law index of $\gamma = 3.08$ for the old metal-poor red giant branch stars out to ~ 300 kpc. It is tempting to argue that this implies that the Milky Way is less massive, with a more quiet accretion history that has been contributed to by a lower number of large mergers than its neighbor M 31 (Bullock & Johnston 2005; Pillepich et al. 2014, 2018). However, it is risky to make broad statements on the history of accretion of these two galaxies with only consideration given to the slope of the outer halo. Indeed, the apparent inconsistency of the slope of the Milky Way stellar halo between different stellar populations necessitates a much more rigorous analysis. It will be interesting to explore these differences further, for example by using a code to generate synthetic stellar populations such as *Galaxia* (Sharma et al. 2011) or the Galactic Besançon Model (Robin et al. 2003). It would also be interesting to compare these results with Milky Way like galaxies in high-resolution cosmological simulations such as *Auriga* (Grand et al. 2017, 2018).

7 SUMMARY

In this paper, we use the new CFIS-*u* survey in combination with PS1 to present a new photometric method to identify BHB stars. This new method reduces contamination from BS by a factor of 1.8 while having a completeness that is at least 1.2 times better than previous methods (Bell et al. 2010; Vickers et al. 2012). We study the completeness of our BHB sample as a function of magnitude and position, and show that our analysis is limited by the depth of the PS1 *z*-band data.

We use the fact that BHB stars have a well-constrained absolute magnitude (Deason et al. 2011) to determine the profile of the outer smooth stellar halo up to a Galactocentric radius of ~ 220 kpc. We

find that the outer stellar halo from 20 to 220 kpc is well reproduced by a broken power law with an inner slope of $\gamma = 4.24 \pm 0.08$, an outer slope $\beta = 3.21 \pm 0.07$ after a radius of $r_b = 41.4^{+2.5}_{-2.4}$ kpc, and a flattening $q = 0.86 \pm 0.02$, close to spherical. This profile is in agreement with the recent measurement of Fukushima et al. (2018) who use BHB stars identified in the HSC-SSP, and with the study of Wan et al. (2018) who use BHB identify in SkyMapper. Although our inner slope is in agreement with the profiles traced by the RR Lyrae (Watkins et al. 2009; Cohen et al. 2017; Hernitschek et al. 2018), the profile of the stellar halo trace by the BHB beyond ~ 40 kpc is significantly shallower than determined with the RR Lyrae that favour a steep single power-law profile.

The variation of the halo profile as a function of stellar populations should be studied further in the future using synthetic stellar populations incorporated into cosmological simulations, to understand if this difference is a consequence of the method to select these different stellar populations, or if it is due to a physical effect. Moreover, in most simulations, the stellar halo has a steeper outer profile than is observed with the BHB (Bullock & Johnston 2005; Pillepich et al. 2014, 2018; Monachesi et al. 2018).

We note that the shallower outer slope that we observe could be a consequence of a poor estimation of the contamination of our BHB sample by the BS. However, we consider this explanation unlikely, since our outer slope is in agreement with the slope found by Fukushima et al. (2018) who use a different method to disentangle the BHB and the BS. Another explanation of a steeper inner slope than the outer slope is that a major merger has let more material in the inner region of the halo than in the outskirts and that the break detected in the BHB profile, which are old stellar population, are the imprint of an old major merger 8–11 Gyr ago as recently proposed by Belokurov et al. (2018) with the *Gaia* data.

ACKNOWLEDGEMENTS

This work is based on data obtained as part of the Canada–France Imaging Survey, a CFHT large program of the National Research Council of Canada and the French Centre National de la Recherche Scientifique. Based on observations obtained with

MegaPrime/MegaCam, a joint project of CFHT and CEA Saclay, at the Canada–France–Hawaii Telescope (CFHT) that is operated by the National Research Council (NRC) of Canada, the Institut National des Sciences de l'Univers (INSU) of the Centre National de la Recherche Scientifique (CNRS) of France, and the University of Hawaii. This research used the facilities of the Canadian Astronomy Data Centre operated by the National Research Council of Canada with the support of the Canadian Space Agency.

We thank the anonymous referee for their careful reading and for their helpful and constructive comments.

R. A. Ibata and N. F. Martin acknowledge support by the Programme National Cosmologie et Galaxies (PNCG) of CNRS/INSU with INP and IN2P3, co-funded by CEA and CNES. This work has been published under the framework of the IdEx Unistra and benefits from a funding from the state managed by the French National Research Agency as part of the investments for the future program.

ES gratefully acknowledges funding by the Emmy Noether program from the Deutsche Forschungsgemeinschaft (DFG).

REFERENCES

- Abadi M. G., Navarro J. F., Steinmetz M., 2006, *MNRAS*, 365, 747
- Aihara H. et al., 2018, *PASJ*, 70, S8
- Amorisco N. C., 2017, *MNRAS*, 469, L48
- Bell E. F. et al., 2008, *ApJ*, 680, 295
- Bell E. F., Xue X. X., Rix H.-W., Ruhland C., Hogg D. W., 2010, *AJ*, 140, 1850
- Belokurov V. et al., 2014, *MNRAS*, 437, 116
- Belokurov V., Erkal D., Evans N. W., Koposov S. E., Deason A. J., 2018, *MNRAS*, 478, 611
- Bernard E. J., et al., 2016, *MNRAS*, 463, 1759
- Bovy J., Rix H.-W., Liu C., Hogg D. W., Beers T. C., Lee Y. S., 2012, *ApJ*, 753, 148
- Bullock J. S., Johnston K. V., 2005, *ApJ*, 635, 931
- Carollo D. et al., 2007, *Nature*, 450, 1020
- Chambers K. C., Magnier E. A., Metcalfe N., Flewelling H. A., Huber M. E., Waters C. Z., 2016, preprint([arXiv:1612.05560](https://arxiv.org/abs/1612.05560))
- Cohen J. G., Sesar B., Bahnholzer S., He K., Kulkarni S. R., Prince T. A., Bellm E., Laher R. R., 2017, *ApJ*, 849, 150
- Conn A. R. et al., 2011, *ApJ*, 740, 69
- Conn A. R. et al., 2012, *ApJ*, 758, 11
- Cooper A. P. et al., 2010, *MNRAS*, 406, 744
- Davidge T. J., McConnachie A. W., Fardal M. A., Fliri J., Valls-Gabaud D., Chapman S. C., Lewis G. F., Rich R. M., 2012, *ApJ*, 751, 74
- De Propriis R., Harrison C. D., Mares P. J., 2010, *ApJ*, 719, 1582
- Deason A. J., Belokurov V., Evans N. W., 2011, *MNRAS*, 416, 2903
- Deason A. J., Belokurov V., Koposov S. E., Rockosi C. M., 2014, *ApJ*, 787, 30
- Farrow D. J. et al., 2014, *MNRAS*, 437, 748
- Foreman-Mackey D., Hogg D. W., Lang D., Goodman J., 2013, *PASP*, 125, 306
- Fukushima T. et al., 2018, *PASJ*, 70, 69
- Goodman J., Weare J., 2010, *Commun. Appl. Math. Comput. Sci.*, 5, 65
- Grand R. J. J. et al., 2017, *MNRAS*, 467, 179
- Grand R. J. J. et al., 2018, *MNRAS*, 474, 3629
- Grillmair C. J., Carlin J. L., 2016, *Astrophysics and Space Science Library*, Vol. 420, *Tidal Streams in the Local Group and Beyond*, Springer-Verlag, Berlin, p. 87
- Harris W. E., 1996, *AJ*, 112, 1487
- Hernitschek N. et al., 2017, *ApJ*, 850, 96
- Hernitschek N. et al., 2018, *ApJ*, 859, 31
- Ibata R. A., Irwin M. J., 1997, *AJ*, 113, 1865
- Ibata R. A. et al., 2014, *ApJ*, 780, 128
- Ibata R. A., et al., 2017, *ApJ*, 848, 128
- Johnston K. V., Bullock J. S., Sharma S., Font A., Robertson B. E., Leitner S. N., 2008, *ApJ*, 689, 936
- Kass R. E., Raftery A. E., 1995, *J. Am. Stat. Assoc.*, 90, 773
- Koposov S. et al., 2007, *ApJ*, 669, 337
- Koposov S. E., Rix H.-W., Hogg D. W., 2010, *ApJ*, 712, 260
- Law D. R., Majewski S. R., 2010, *ApJ*, 714, 229
- Lenz D. D., Newberg J., Rosner R., Richards G. T., Stoughton C., 1998, *ApJS*, 119, 121
- Libeskind N. I., Knebe A., Hoffman Y., Gottlöber S., Yepes G., 2011, *MNRAS*, 418, 336
- Majewski S. R., Skrutskie M. F., Weinberg M. D., Ostheimer J. C., 2003, *ApJ*, 599, 1082
- Malhan K., Ibata R. A., Martin N. F., 2018, *MNRAS*, 481, 3442
- Martin N. F., Ibata R. A., McConnachie A. W., Mackey A. D., Ferguson A. M. N., Irwin M. J., Lewis G. F., Fardal M. A., 2013, *ApJ*, 776, 80
- Martínez-Delgado D. et al., 2010, *AJ*, 140, 962
- Monachesi A. et al., 2018, preprint([arXiv:1804.07798](https://arxiv.org/abs/1804.07798))
- Pila-Díez B., de Jong J. T. A., Kuijken K., van der Burg R. F. J., Hoekstra H., 2015, *A&A*, 579, A38
- Pillepich A. et al., 2014, *MNRAS*, 444, 237
- Pillepich A. et al., 2018, *MNRAS*, 475, 648
- Preston G. W., Shectman S. A., Beers T. C., 1991, *ApJ*, 375, 121
- Rix H.-W., Bovy J., 2013, *Astron. Astrophys. Rev.*, 21, 61
- Robin A. C., Reylé C., Derrière S., Picaud S., 2003, *A&A*, 409, 523
- Schlafly E. F., Finkbeiner D. P., 2011, *ApJ*, 737, 103
- Schlegel D. J., Finkbeiner D. P., Davis M., 1998, *ApJ*, 500, 525
- Schönrich R., Asplund M., Casagrande L., 2011, *MNRAS*, 415, 3807
- Sesar B. et al., 2017, *AJ*, 153, 204
- Sharma S., Bland-Hawthorn J., Johnston K. V., Binney J., 2011, *ApJ*, 730, 3
- Sirko E. et al., 2004, *AJ*, 127, 914
- Slater C. T., Nidever D. L., Munn J. A., Bell E. F., Majewski S. R., 2016, *ApJ*, 832, 206
- Thomas G. F., Famaey B., Ibata R., Lüghausen F., Kroupa P., 2017, *A&A*, 603, A65
- Vickers J. J., Grebel E. K., Huxor A. P., 2012, *AJ*, 143, 86
- Wan Z., Kafle P. R., Lewis G. F., Mackey D., Sharma S., Ibata R. A., 2018, *MNRAS*, 480, 1218
- Watkins L. L. et al., 2009, *MNRAS*, 398, 1757
- Xue X. X. et al., 2008, *ApJ*, 684, 1143
- Xue X.-X. et al., 2011, *ApJ*, 738, 79
- Xue X.-X., Rix H.-W., Ma Z., Morrison H., Bovy J., Sesar B., Janesh W., 2015, *ApJ*, 809, 144
- Yanny B. et al., 2000, *ApJ*, 540, 825

This paper has been typeset from a $\text{\TeX}/\text{\LaTeX}$ file prepared by the author.